ORIGINAL RESEARCH ARTICLE

Characterization and Modeling of Wear Behavior of AISI D3 Tool Steel under Dry Sliding Conditions

Faruk Çavdar

In this study, central composite design (CCD) and response surface methodology (RSM) were employed to model the wear behavior of AISI D3 tool steel. The objective was to investigate the variation of the coefficient of friction (COF), wear track depth and width, volume loss, and wear rate (WR) under different experimental conditions, including loads (L) ranging from 1 to 20 N, sliding speeds (s) between 100 and 250 mm/s, and sliding distances (D) from 100 to 500 m. To achieve this, a CCD-based experimental design was implemented, and the designed experiments were conducted using pin-on-disc dry sliding tests. Variance analyses revealed that COF was influenced by both the applied load and sliding speed, while the sliding distance showed no statistically significant effect. Based on the regression model, a 3D graph indicated that the lowest COF value of 0.35 would be observed at a sliding speed of 250 mm/s under both 1 and 20 N loads, while the highest COF value of 1.4 would occur at a sliding speed of 100 mm/s under a 1-N load. Additionally, 3D plots generated for WR suggested that WR approached zero for load values between 10 and 17 N, a sliding speed of 125 mm/s, and a sliding distance of 100 m. The highest WR value was observed under the conditions of 250 N load, 250 mm/s sliding speed, and 100 m sliding distance. Furthermore, SEM images and EDS analysis were conducted on the worn surface and abrasive ball, revealing that oxidation resulting from localized heating played a crucial role in the wear behavior.

1. Introduction

Steels are iron-carbon (Fe-C) alloys with varying carbon content. They can be classified into two main categories: non-alloy steels and alloy steels (Ref 1). Alloy steels are further divided into low alloy and high alloy steels. Among the high alloy steels, tool steel stands out due to its unique properties and exceptional performance in demanding working conditions. Despite its relatively small production volume compared to other steel types, tool steel plays a strategic role in the manufacturing of components made from different steel grades and engineering materials (Ref 2, 3). The significance of tool steel in various industries has prompted extensive research to enhance production techniques and explore its applications in diverse fields (Ref 3).

Tool steels are vital for the production of tools, molds, and machine parts used in shaping processes like forging, cutting, drilling, and bending. They offer high wear resistance, hardness, toughness, heat resistance, machineability, hardenability, and a homogeneous microstructure. These steels excel in maintaining performance at different temperatures and speeds without deformation, breakage, or excessive wear (Ref 4). Alloying elements such as chromium, molybdenum,

vanadium, tungsten, and cobalt, along with additives like manganese, nickel, silicon, and grain-refining elements such as aluminum, titanium, and zirconium, contribute to their superior properties. It is essential to limit impurities like phosphorus and sulfur to below 0.03% (Ref 5). Tool steels are widely used across industries for their exceptional attributes, enhancing productivity and enabling the fabrication of high-quality components.

Tool steels are available in over 500 different compositions and properties. They are classified into seven groups by AISI and SAE based on quenching media and application areas. The groups include water quenching (W), shock resistant (S), cold work (O, A, D), hot work (H), high speed (T, M), plastic mold (P), and special purpose tool steels (Ref 6). The life cycle of tool steel depends on the design, working conditions, and steel selection (Ref 7).

Cold work tool steels have broad applications for shaping workpieces below 200 °C through machining or forming processes. They are crucial in industries requiring precise shaping, contributing to enhanced productivity and high-quality outcomes.

AISI D type steel, also known as high carbon and high chrome cold work tool steel, contains approximately 1.4-2.5% carbon and about 12.0% chromium. This type of steel also includes vanadium, molybdenum, wolfram, nickel, and manganese. However, cobalt, which enhances mechanical resistance at high temperatures, is not present in these steels due to its high cost. AISI D type steels generally exhibit high wear resistance (Ref 5).

The wear characteristics of materials are of significant importance in the design and selection of materials for components that experience relative sliding or rotational motion with contacting surfaces, such as machine parts and molds.

Faruk Çavdar, Department of Machinery and Metal Technologies, Osmaniye Vocational School, Osmaniye Korkut Ata University, Osmaniye, Turkey. Contact e-mail: farukcavdar@osmaniye.edu.tr.

Wear testing serves the purpose of assessing the suitability of a material for applications involving wear, evaluating the potential of surface engineering techniques to mitigate wear in specific scenarios, and investigating the wear properties of materials by studying the impact of process conditions and material parameters on wear performance (Ref 8, 9). Over the years, researchers have conducted extensive studies on the wear behavior of both bulk materials (Ref 10-14) and coatings applied to base materials (Ref 15-20). While many of these studies have traditionally employed conventional evaluation methods, recent research has focused on utilizing statistical techniques like response surface methodology to mathematically model the influence of parameters on wear behavior (Ref 21-26). This approach enables the prediction of wear behavior within the experimental parameter space, even for untested parameter combinations, thereby providing valuable insights into wear analysis.

Among the various D type tool steels, AISI D3 stands out as a widely utilized material in applications that demand exceptional resistance against wear, pressure, and abrasion (Ref 27). Consequently, it becomes imperative to comprehensively investigate the wear behavior of this material under typical operating conditions but the wear behavior of AISI D3 has not been investigated in any publication. Therefore, in this study, an experimental investigation was conducted to examine the wear performance of AISI D3 steel under a range of loads spanning from 1 to 20 N, sliding speeds varying from 100 to 250 mm/s, and sliding distances extending from 100 to 500 m. Furthermore, the wear characteristics of AISI D3 were modeled within the defined operating ranges using the response surface methodology. As a result, the wear behavior parameters, including the coefficient of friction, wear track depth, wear track width, volume loss, and wear rate, can be accurately predicted for any combination of parameter values falling within the scope of this study.

2. Materials and Methods

In this study, AISI D3 specimens with nominal chemical composition given in Table 1 are utilized. The specimens were prepared by cutting in $25 \times 25 \times 2.5$ mm dimensions by using a high-speed precision cutting device and grinding to get surface quality $R_a < 0.2$.

2.1 Statistical Experimental Design

The most effective parameters in the dry sliding test are assumed to be applied load (L), sliding speed (s), and sliding distance (D) in this study. The experiments were carried out at room temperature because AISI D3 tool steel is designed to work at temperatures below 150 °C. Wear characteristics modeled in this study are coefficient of friction (COF) width (w) and depth (d) of wear track, volume removal (V), and wear rate (WR) under specified conditions.

A central composite design has been applied to the independent variables (parameters) with minimum and maximum values of 100 and 250 mm/s for s, 1 and 20 N for L, 100 and 500 m for D. Set values of these parameters obtained from CCD and corresponding maximum contact pressure, maximum shear stress, and contact radius values for each experiment are listed in Table 2.

Table 1 Theoretical chemical composition (wt.%) of AISI D3 tool steel

C	Mn	Si	Ni	Cr	P	S	V	Fe
2.10	0.30	0.25	0.30	11.50	0.03	0.03	1.0	Balance

2.2 Wear Tests

Ball on disc type, Turkyus POD&HT&WT model wear test machine was used to perform dry sliding wear tests. Experiments were conducted at room temperature, and the wear track diameter was kept constant at 8 mm for each experiment.

In the studies, abrasive balls with a diameter of 6.0 mm made of ASTM 52100 ball-bearing steel were employed.

During wear tests, COF was recorded continuously by means of the software of the wear test device. COF plots were created against time by using software records. The average of the whole COF values of each test was used for statistical analysis.

Width and depth of wear tracks were determined by contour profiles obtained using a 2-D profilometer. Based on the fact that the wear trace is half of the ellipse as shown in Fig. 1, the wear track area, wear volume losses, and specific wear rates were calculated using Eq 1, 2, and 3 as stated in the previous studies (Ref 19, 25, 28)

$$A = 0.25\pi w d \tag{Eq 1}$$

$$V = 2\pi r A \tag{Eq 2}$$

$$WR = \frac{V}{LD} \tag{Eq 3}$$

where, A is the area of the wear track, V is the volume of the wear track, r is radius of the wear track, w is the average wear track width, D is the average wear track depth, L is the test load, D is the sliding distance, and WR is the specific wear rate.

2.3 Construction of Response Surface Models

Set values of experiments given in Table 2 were used to conduct dry sliding wear tests, after which measurements were taken on wear samples. The overall variation of the test results with the factors was analyzed using analysis of variance on dependent variables. Polynomial regression models for each response were constructed as a result of ANOVA. The degrees of the model are determined by trial and error. The models with higher significance, R^2, and R^2_{adj} values were chosen for the construction of response surfaces of the dependent variables.

Design expert statistical software was used to conduct statistical procedures. Change in each response variable with respect to change in the independent variables is visualized and interpreted by using 3-D response surfaces constructed according to the response models.

3. Results

Results of ANOVA studies for responses, i.e., coefficient of friction, wear tack width, wear track depth, volume loss, and wear rate are presented in Table 4. The ratio of explained variation to unexplained variance is determined by the F value

Table 2 Set values of independent variables for each experiment and corresponding contact properties

| Exp. no.	s, mm/s	L, N	D, m	Max. contact pressure, GPa	Max. shear stress, MPa	Depth of max. shear stress, μm	Contact radius, μm
E1	130.41	4.85	181.08	686.00	214.40	27.56	58.10
E2	175.00	10.50	300.00	887.40	277.35	35.66	75.16
E3	219.60	16.15	418.92	1024.00	320.20	41.16	86.76
E4	175.00	10.50	300.00	887.40	277.35	35.66	75.16
E5	175.00	10.50	300.00	887.40	277.35	35.66	75.16
E6	130.41	16.15	418.92	1032.00	320.20	41.16	86.76
E7	130.41	4.85	418.92	686.00	214.40	27.56	58.10
E8	175.00	1.00	300.00	405.20	126.65	16.28	34.33
E9	175.00	10.50	300.00	887.40	277.35	35.66	75.16
E10	219.60	4.85	181.08	686.00	214.40	27.56	58.10
E11	175.00	20.00	300.00	1100.00	343.85	44.20	93.17
E12	175.00	10.50	500.00	887.40	277.35	35.66	75.16
E13	219.60	4.85	418.92	686.00	214.40	27.56	58.10
E14	219.60	16.15	181.08	1024.00	320.20	41.16	86.76
E15	175.00	10.50	100.00	887.40	277.35	35.66	75.16
E16	130.41	16.15	181.08	1024.00	320.20	41.16	86.76
E17	250.00	10.50	300.00	887.40	277.35	35.66	75.16
E18	175.00	10.50	300.00	887.40	277.35	35.66	75.16
E19	175.00	10.50	300.00	887.40	277.35	35.66	75.16
E20	100.00	10.50	300.00	887.40	277.35	35.66	75.16
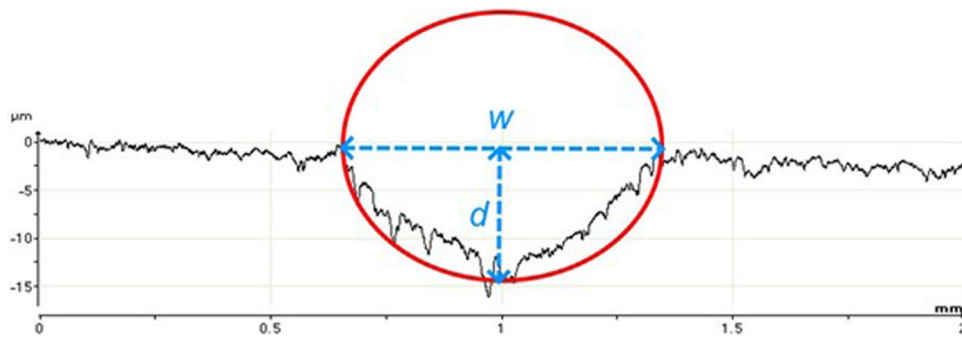
Fig. 1 Calculation of wear track area by using profilometer plots

of the model or a term. A model or term is considered significant if its F value exceeds the critical F value in the 95 percent confidence range. Examining p values is another method for determining the model's and terms' relevance. The model or a term is assumed to have a significant impact on the response if the p value is small enough (under 0.05 for the model and 0.1 for a term) (Ref 29).

The correlation coefficient (R^2) is a statistical index that expresses the percentage of variance in a dependent variable that is explained by one or more independent variables in a regression model. However, a high R^2 value does not automatically indicate a strong regression model. Because including a new variable in the model always raises the R^2 value, regardless of whether the variable is statistically significant. Therefore, adjusted R^2 (R^2_{adj}) is employed alongside or in place of R^2 in the majority of statistical applications. When a necessary term is added to the model, the R^2_{adj} value rises; conversely, when an unneeded term is introduced, this value falls. R^2 and R^2_{adj} values are anticipated to be in close proximity in a sound model (Ref 29, 30).

3.1 Coefficient of Friction (COF)

A reduced cubic model has been developed for COF by using dependent and corresponding response values listed in Table 3. It is seen in ANOVA tables (Table 4) that, F value and p value of the model are 6.59 and 0.0024, respectively which means the model is significant in the reliability of 95% according to F distribution tables (Ref 31). The only individual factor having a significant effect on the COF is L with p value of 0.0037. The term s is contained in the model because of hierarchy although it has p value greater than 0.1. The interaction factor terms L^2, sL^2, and sL have significant effects on COF.

The response model constructed for COF has R^2 and R^2_{adj} values of 0.7 and 0.6, respectively. This implies the model is not too strong to represent a response. But R^2_{adj} value is in the range of $0.8*R^2$ and this means the model contains no redundant terms. In some cases, it is impossible to construct a robust mathematical model of wear mechanisms because they involve numerous uncontrollable agents (Ref 26).

Table 3 Experimental set values of independent parameters and results of experiments

Exp. no.	s, mm/s	L, N	D, m	COF	w, μm	d, μm	V, mm^3	WR, (mm^3/Nm)*10^{-6}
E1	130.41	4.85	181.08	0.87	643.00	9.08	0.1164	132.55
E2	175.00	10.50	300.00	0.71	762.25	12.56	0.1911	60.66
E3	219.60	16.15	418.92	0.65	1500.50	8.28	0.2448	36.19
E4	175.00	10.50	300.00	0.61	869.00	15.67	0.2724	86.48
E5	175.00	10.50	300.00	0.63	759.25	14.79	0.2204	69.97
E6	130.41	16.15	418.92	0.62	1001.50	20.17	0.3972	58.71
E7	130.41	4.85	418.92	0.92	1190.50	10.10	0.2341	115.21
E8	175.00	1.00	300.00	0.83	481.75	2.56	0.0320	106.75
E9	175.00	10.50	300.00	0.57	907.00	18.03	0.3234	102.68
E10	219.60	4.85	181.08	0.77	638.00	12.69	0.1584	180.29
E11	175.00	20.00	300.00	0.70	1330.50	11.90	0.3012	50.19
E12	175.00	10.50	500.00	0.61	832.00	7.74	0.1135	21.62
E13	219.60	4.85	418.92	0.57	842.00	5.92	0.0683	33.62
E14	219.60	16.15	181.08	0.59	1355.50	10.23	0.2714	92.83
E15	175.00	10.50	100.00	0.60	558.50	7.14	0.0797	75.94
E16	130.41	16.15	181.08	0.61	725.50	8.70	0.1273	43.54
E17	250.00	10.50	300.00	0.71	1063.50	24.25	0.5266	167.18
E18	175.00	10.50	300.00	0.51	830.50	22.32	0.3655	116.04
E19	175.00	10.50	300.00	0.69	827.75	20.76	0.3300	104.76
E20	100.00	10.50	300.00	0.60	478.00	5.38	0.0542	17.22

Table 4 Results of ANOVA and correlation coefficients for responses

Source	Coefficient of friction		Wear track width		Wear track depth		Volume loss		Wear rate	
	F value	p value	F value	p value	F value	p value	F value	p value	F value	p value
Model	6.59	0.0024	21.79	< 0.0001	6.62	0.0027	10.96	0.0003	8.82	0.0011
s	1.28	0.2762	27.23	0.0008	16.10	0.0020	34.10	0.0001	25.55	0.0005
L	12.13	0.0037	57.22	< 0.0001	4.23	0.0641	18.78	0.0012	17.63	0.0018
D	...	...	31.00	0.0005	0.15	0.7050	2.40	0.1494	14.66	0.0033
sL	5.46	0.0349	43.64	0.0002	1.08	0.3205	0.51	0.4897	1.04	0.3311
sD	...	...	4.47	0.0674	5.09	0.0454	9.71	0.0098	11.49	0.0069
LD	...	...	...	...	...	...	...	...	4.27	0.0658
s^2	...	...	0.73	0.4189	...	...	...	...	...	...
L^2	8.87	0.0100	1.53	0.2510	13.90	0.0033	6.14	0.0307	0.0676	0.8001
D^2	...	...	4.07	0.0783	13.27	0.0039	17.04	0.0017	4.70	0.0553
s^2L	...	...	4.62	0.0639	...	...	...	...	...	...
sL^2	5.47	0.0347	3.13	0.1147	14.58	0.0029	24.95	0.004	15.57	0.0028
s^2L^2	...	...	19.99	0.0021	...	...	...	...	...	...
Lack of fit	0.70	0.6959	3.28	0.1166	0.633	0.7048	0.46	0.8117	0.8882	0.5502
R^2		0.70		0.96		0.83		0.89		0.89
R^2_{adj}		0.60		0.92		0.70		0.81		0.79

Table 5 provides the regression coefficients for the COF model in terms of coded and real components. The size of coefficients in terms of coded factors shows the relative effect of that term in the regression model. The most effective term is sL^2 and the least effective term is s. The value of the sliding distance does not influence on COF according to the model.

The developed response model through coefficients in terms of actual factors in Table 4 is stated in Eq 4. Relationships between the calculated values using response model equations and measured values are plotted in Fig. 2. In Fig. 2(a), it can be seen that the points do not diverge too far from the 45-degree line. Therefore, the modeling results can be considered adequately representative of the actual measurements.

$$COF = 0.6335 + 0.0236s - 0.645L + 0.0565sL + 0.0532L^2 - 0.0879sL^2$$

(Eq 4)

3.2 Wear Track Width (w)

Wear track width response was created using a reduced quartic model with 11 terms. As can be seen in Table 3, the model's p value is less than 0.001 and its F value is 21.79, respectively. The model's significance is inferred from F value with F-statistic tables. Additionally, according to the p value,

Table 5 Regression coefficients of coded and actual COF model terms

Factor	Coefficient in terms of coded factor	Coefficient in terms of actual factor	% Effect on the response
Constant	0.6335	2.4130	…
s	0.0326	− 0.00846	11.06
L	− 0.645	− 0.31264	21.89
sL	0.0565	0.00152	19.17
L^2	0.0532	0.01248	18.05
sL^2	− 0.0879	− 0.000062	29.83

the likelihood that the model is not significant is less than 0.01%.

The response model of w has R^2 and R^2_{adj} values of 0.97 and 0.92, respectively. These values imply the model represents change in response in a good way, and the model has no redundant terms.

Table 6 displays the regression coefficients of w for the coded and actual components. L, which has a weight of 20.12% on worn track width, is the most useful individual factor. It is followed by s and D, which have weights of 13.88 and 9.53%, respectively. While D has a positive influence on the response, s and L have a negative impact on the response w.

The response model developed by using actual terms coefficients is listed in Table 6 and is stated in Eq 5. The distribution of predicted versus measured values of wear track area is shown in Fig. 2(b). Distribution of the points on the table is homogeneous, and the points are distributed quite closely to the 45-degree line on the plot. This shows a good fit of the model to the real case.

$$w = 13927.89 - 154.34s - 2568.91L + 4.92D + 27.78sL - 0.01sD + 0.42s^2 + 106.17L^2 - 0.0032D^2 - 0.074s^2L - 1.15sL^2$$

(Eq 5)

3.3 Wear Track Depth (d)

The reduced cubic response model for d consists of 8 terms, and the F value and p value are 6.62 and 0.0027, respectively. These values show that the model is significant. Individual terms s and L significantly affect the model, whereas d has little meaningful effect.

R^2 and R^2_{adj} values of the d model are 0.83 and 0.70, respectively. This means the model is strong enough to represent response, and no redundant terms are included in the model (Ref 32, 33).

Table 7 lists the regression coefficients for the coded and real components. With a 22.38 percent effect, sL^2 is the most efficient term. Equation 6 is the response model equation for d generated using the coefficients of the real factors. Figure 2(c)'s predicted versus actual distribution graph shows that the majority of the points are situated close to the 45-degree line. It might be argued that the model accurately depicts real-world situations.

3.4 Volume Loss (V)

For volume loss, a reduced cubic model with 8 terms was created. The F value and p value, which have values of 10.96 and 0.0003, respectively, confirm the model's significance. Individual factors having significant impact on the model are s and L. Despite the fact that its impact on it is not immediately apparent, d is included in the model because hierarchy is essential.

Because R^2 and R^2_{adj} have values of 0.89 and 0.81, respectively, it can be said that the model effectively describes the measurement results and does not contain extraneous terms.

$$d = 18.421 - 0.214sL - 14.697L + 0.225D + 0.098sL - 0.001sD + 0.756L^2 + 0.0002D^2 - 0.005sL^2$$

(Eq 6)

The regression coefficients for the model are displayed in Table 8 in both coded and real terms. In terms of the individual terms of the models, s has the highest influence, with 24.85%. The most impactful interaction term is sL^2, which has a 27.78% impact.

The regression model of volume loss which is constructed by using regression coefficients in terms of actual terms in Table 8 is stated in the equation. Figure 2(d) displays the distribution of predicted versus actual wear track area values. The points are dispersed uniformly across the table and are positioned somewhat near the 45-degree line on the plot. This demonstrates how well the model matches the actual case.

$$V = 0.639944 - 0.006048s - 0.379076L + 0.004908D + 0.002374sL - 0.000012sD + 0.018139L^2 - 0.00000438D^2 - 0.00011sL^2$$

(Eq 7)

3.5 Wear Rate (WR)

A simplified cubic model with 9 terms was developed for wear rate response. The model's significance is confirmed by the F value and p value, which have values of 8.82 and 0.0011, respectively. All individual components (s, L, and D) have a significant impact on the model.

Considering that R^2 and R^2_{adj} have values of 0.89 and 0.79, respectively, it can be concluded that the model accurately represents the results of the measurement and does not include any unnecessary variables.

Regression coefficients of the wear rate response model in terms of coded and actual components are presented in Table 9. The most effective model term is sL^2 included in the volume loss model. On the other hand, s is the most effective individual term in the model.

The mathematical model of the WR is constructed by regression coefficient in terms of actual factors and formulated in Eq 8. It can be stated that the points in Fig. 2(e) which is the plot of actual versus predicted distribution of WR scattered homogeneous and near the $y = x$ line. So that the model represents real cases fairly well.

$$WR = 430.77 - 1.41661s - 132.816L + 0.914D + 0.701sL - 0.00474sD + 0.0228LD + 5.547L^2 - 0.00084D^2 - 0.03196sL^2$$
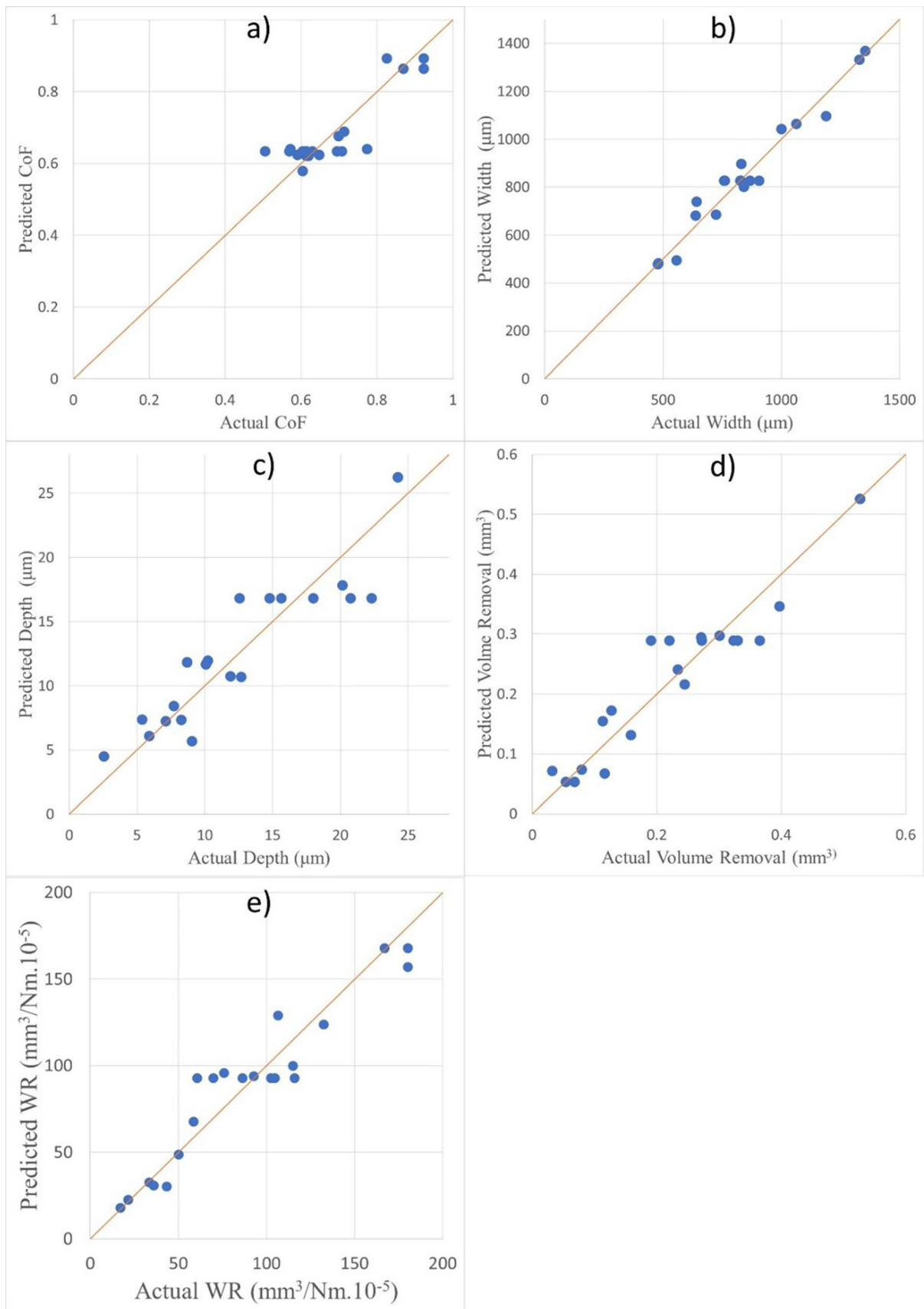
(Eq 8)

Fig. 2 Actual vs. predicted values distribution plot for (a) COF, (b) width, (c) depth, (d) volume removal, and (e) wear rate

Table 6 Regression coefficients of coded and actual width model terms

Factor	Coefficient in terms of coded factors	Coefficient in terms of actual factors	% Effect on the response
Constant	825.96	13927.89	…
s	174.07	− 154.34	13.88
L	252.33	− 2568.91	20.12
D	119.53	4.92	9.53
sL	185.31	27.78	14.78
sD	− 59.31	− 0.01	4.73
s^2	− 19.52	0.42	1.56
L^2	28.34	106.17	2.26
D^2	− 46.21	− 0.0032	3.69
s^2L	− 93.65	− 0.074024	7.47
sL^2	− 77.13	− 1.15	6.15

Table 7 Regression coefficients of coded and actual wear track depth model terms

Factor	Coefficient in terms of coded factors	Coefficient in terms of actual factors	% Effect on the response
Constant	16.8	18.421	…
s	5.61	− 0.214	22.38
L	1.85	− 14.697	7.38
D	0.3497	0.225	1.39
sL	− 1.22	0.098	4.87
sD	− 2.65	− 0.001	10.57
L^2	− 3.25	0.756	12.96
D^2	− 3.17	0.0002	12.64
sL^2	− 6.97	− 0.005	27.80

Table 8 Regression coefficients of coded and actual volume loss model terms

Factor	Coefficient in terms of coded factors	Coefficient in terms of actual factors	% Effect on the response
Constant	0.2891	0.639944	…
s	0.1404	− 0.006048	24.85
L	0.0671	− 0.379076	11.87
D	0.024	0.004908	4.25
sL	0.0145	0.002374	2.57
sD	− 0.063	− 0.000012	11.15
L^2	− 0.0372	0.018139	6.58
D^2	− 0.0619	− 4.38E-06	10.95
sL^2	− 0.157	− 0.00011	27.78

4. Discussions

4.1 Coefficient of Friction (COF)

Oxides have a significant impact on the coefficient of friction and wear volume loss. Oxides are hard compounds formed as a result of the affinity of metallic elements to oxygen during the wear process in an open-air environment (Ref 34, 35). Heating due to friction during the wear process accelerates the formation of oxides. If the formed oxides do not fracture during the wear process, they exhibit lubricating effects, leading to a decrease in the coefficient of friction and wear volume loss (Ref 34-36). However, if they fracture during wear, their hard nature can cause three-body abrasion, resulting in an increased coefficient of friction and wear volume loss due to their entrapment between the abrasive ball and the substrate (Ref 18).

Figure 3 illustrates the change in COF with sliding distance over time during wear testing. Figure 3(a) shows a slight reduction in COF as the sliding speed increases from 100 to 200 mm/s, but it increases again at 250 mm/s. The formation of an oxide layer on the surface explains the initial decrease in COF with increased speed, while the breakdown of the oxide layer and exposure of the underlying surface contribute to the COF increase at 250 mm/s. The influence of load on COF, depicted in Fig. 3(b), indicates a slight increase in COF with increasing load up to 4.85 N. The absence of significant surface shear stress and temperature changes within this load range prevents the formation and breakdown of the oxide layer. However, at higher loads, the oxide layer formation mechanism successfully reduces COF until the load value reaches 20 N, resulting in a slight increase in friction. Figure 3(c) indicates that the COF variation with sliding distance exhibits random behavior, likely influenced by speed and load rather than distance alone.

Table 9 Regression coefficients of coded and actual WR model terms

Factor	Coefficient in terms of coded factors	Coefficient in terms of actual factors	% Effect on the response
Constant	92.74	430.77	...
s	44.58	− 1.41661	22.63
L	− 23.84	− 132.81632	12.10
D	− 21.73	0.91354	11.03
sL	7.58	0.70112	3.85
sD	− 25.14	− 0.00474	12.76
LD	15.32	0.02280	7.78
L^2	− 1.43	5.54725	0.73
D^2	− 11.93	− 0.00084	6.06
sL^2	− 45.47	− 0.03196	23.08

Figure 4, a 3-D representation, demonstrates a linear decrease in COF with steep slopes at low load values as speed increases. The slope flattens as the load reaches 10 N, and at this load, COF slightly increases with speed. At 20 N load, COF decreases linearly with increasing speed but not as significantly as at lower loads due to reduced contact between surfaces. When evaluating COF variation with load at constant speeds, it follows a parabolic trend, with the lowest point at 12.5 N and a COF of 0.55. Despite increasing velocity values, COF remains constant at 0.65. However, as velocity approaches 250 mm/s, COF exhibits an inverted parabolic shape with a peak at 11.5 N and a COF of 0.69. These findings suggest that an oxide layer forms at speeds above 200 mm/s for load values ranging from 1 to 20 N, except at the 12.5 N load.

4.2 Wear Track Depth (d)

Figure 5 presents 3-D graphs illustrating the relationship between wear track depth, sliding speed, and load at a fixed sliding distance and load. Figure 5(a) shows an increasing trend in depth (d) with higher speeds over a 150-m distance. The steepest increase occurs at 11 N load, while the slope gradually flattens as the load decreases to 5 N and increases to 16 N. At low sliding speeds, both 5 N and 16 N loads result in increasing depth, forming a parabolic shape with a minimum point at 10.5 N load. At a speed of 250 mm/s, the behavior changes to an inverted parabolic shape, with a maximum depth of 11 N load and a decrease from 26 to 12 μm. In Fig. 5(b), with a sliding distance of 300 m, the depth variation follows a similar pattern as in the previous graph. However, there is an increase in the parabolic base value at a sliding speed of 120 mm/s, ranging from 0.5 to 9 μm. Figure 5(c) depicts the depth variation as a function of load and sliding speed at a sliding distance of 450 m. The behavior is similar to Fig. 5(a) and (b) but with a smaller maximum depth of 16 μm. A parabolic variation is observed in the 120 mm/s speed range, as seen in Fig. 5(b).

Figure 5d, e, and f represents the response surfaces of track depth for constant loads of 3, 10, and 17 N, respectively. For a load of 3 N in Fig. 5(d), depth decreases linearly with increasing speed. The slope becomes steeper as the distance increases, following an inverted parabolic trend from 140 to 380 m. In Fig. 5(e), the depth increases linearly with speed at a load of 10 N. The slope becomes less steep as the distance increases, and a parabolic increase in depth is observed from 140 to 380 m. Figure 5(f) demonstrates an inversely proportional relationship between depth and speed at a load of 17 N.

The slope of the narrowing track width increases with distance, as shown in Fig. 5(d). However, the parabolic change in track width with increasing distance persists at this load.

4.3 Wear Track Width (w)

Figure 6 illustrates the relationship between wear track width, sliding speed, load, and sliding distance. In Fig. 6(a), the track width varies parabolically with varying load and speed for a fixed distance. The parabolic shape moves its base point as the load and speed change. Similarly, Fig. 6(b) and (c) shows parabolic variations in track width with different load and speed combinations for fixed distances.

Figure 6(d) demonstrates how track width varies with sliding distance and speed under a 3-N load. The track width increases parabolically toward specific speed points, while the inverse parabolic relationship is observed between width and distance. Figure 6(e) shows that under a 10 N load, changes in distance and speed have less impact on track width, with a linear increase in width as speed rises. Figure 6(f) illustrates a parabolic increase in track width with speed under a 17-N load, while the relationship with distance follows an inverted parabolic pattern. In summary, the graphs depict the complex interactions between sliding speed, load, distance, and wear track width, showcasing various parabolic and linear relationships.

4.4 Volume Loss (V)

Figure 7 presents the variation in volume loss with shear rate and load for constant distance and load values. Figure 7(a) shows that volume loss increases linearly with speed, reaching a peak at 11 N load. At lower speeds, the volume loss follows a parabolic pattern with load, while at higher speeds, it decreases inversely parabolically. Similar behavior is observed in Fig. 7(b), where the parabolic pattern shifts to higher values. Figure 7(c) shows consistent volume behavior at low speeds but varies with distance at high speeds.

In Figure 7e, volume loss increases linearly with speed for a 10-N load, with an inverse parabolic relationship between volume and distance. Figure 7(f) demonstrates a reduction in volume loss with the increasing speed at high speeds (> 17 N load), while the volume remains constant at low speeds. The volume loss follows a reverse parabolic pattern at different distances. In summary, the graphs depict the relationship between volume loss, shear rate, load, and sliding distance. They demonstrate linear, parabolic, and inverse parabolic
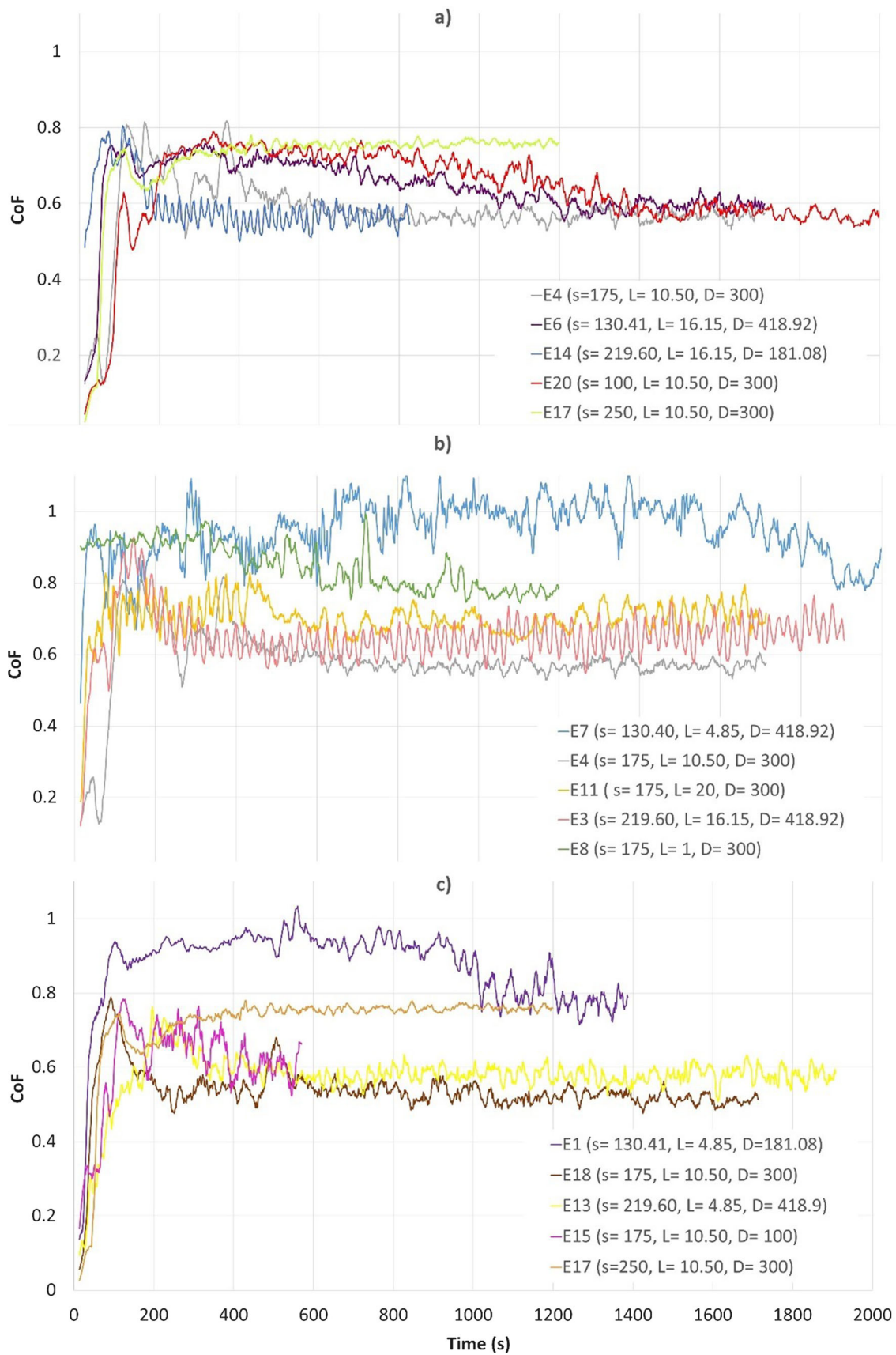
Fig. 3 COF-time graphs with respect to (a) changes in sliding speed, (b) changes in load, and (c) changes in distance (plotted by using experimental values)
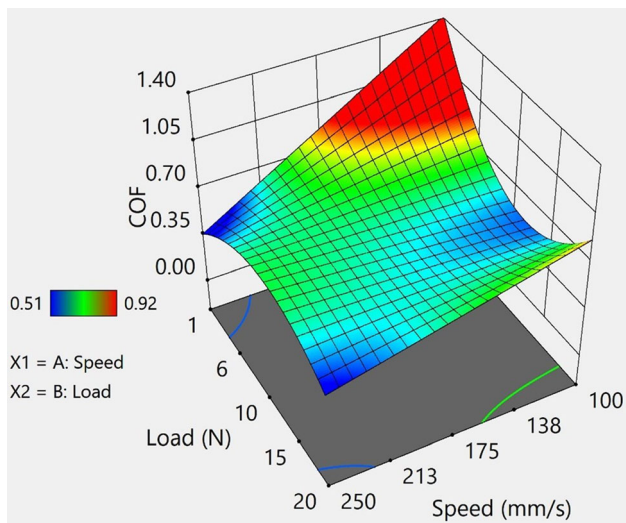
Fig. 4 3-D response surface plot of COF model

relationships, with variations depending on speed and load values.

4.5 Wear Rate (WR)

Figure 8 displays the variation of wear rate at constant distance and load. In Fig. 8(a), wear rate increases linearly with speed, with a steeper slope at higher loads. At low speeds, the wear rate follows a parabolic pattern with load, with a base point at 13.8 N and 10.2 wear rate. Figure 8(a), (b), and (c) presents the 3D response surface of wear rate for constant load values based on speed and distance.

In Figure 8d, at a constant load of 3 N and 100 m distance, the wear rate remains unchanged with speed. However, the wear rate inversely varies with speed as distance increases. At 125 mm/s and 230 m distance, the wear rate reaches a high value of 176.8, then decreases parabolically from 100 to 360 m at a speed of 250 mm/s. For a constant load of 10 N in Fig. 8(e), the wear rate increases proportionally with speed, with a steeper slope as distance increases. Wear rate peaks at 330 m and 46.8 wear rate at 125 mm/s speed, then decreases in an inverse parabolic pattern. At 250 mm/s speed, wear rate decreases from 243 to 132 over a distance range of 100-360 m. Figure 8(f) shows that the wear rate decreases with increasing speed at short distances and low slopes under a 17-N load. However, as distance increases, wear rate increases in direct proportion to speed. At low speeds like 125 mm/s, the wear rate increases in a reverse parabolic pattern with distance. Conversely, at high speeds like 250 mm/s, the wear rate decreases inversely parabolically with distance. In summary, the graphs illustrate the relationship between wear rate, distance, load, and sliding speed. They depict linear, parabolic, inverse parabolic, and proportional relationships, with variations based on load, speed, and distance values.

4.6 Failure Mechanisms

SEM image and EDS analysis of the sample surface subjected to sliding test according to parameters E10 (s = 219.6 mm/s, L = 4.85 N, D = 181.08 m) in Table 3 are shown in Fig. 9. It is possible to infer from this surface appearance that the principal wear mechanisms are severe

plastic deformation and oxidation mechanisms. Because it is evident that the material is being removed at a rapid rate (Pt 2) along the surface, and there are black flat surfaces and areas where the worn particles have been squeezed and extruded between the ball and the substrate (Pt 1). EDS analysis highlights high oxygen concentration (about 30%), particularly at Pt 1. The areas in the image that resemble this are those that are subjected to repeated loads the most; they are smoother in structure and have darker colors depending on the amount of oxide present. On the other hand, the Pt 2 and Pt 3 regions show the presence of oxide fragments that are separated from the surface by the impact of friction as well as an oxide layer that immediately regenerates in these areas. Depending on the applied force and shear stress between the interacting surfaces, temperature increases occur suddenly at the sample contact locations. The rate of surface oxidation accelerates as the temperature rises (Ref 35, 37). The chemical composition of the samples has a direct impact on the oxide layer that forms on the surface as well as the samples' capacity to stick to surfaces. Once more, the oxides on the left side of the image are extruded in the direction of wear.

SEM and EDS photographs of the abrasion track area of test sample E18, which was evaluated at 175 mm/s sliding speed, 0.5 N load, and 300 m sliding distance, are shown in Fig. 10. This SEM view also shows the oxidation process. It can be seen that the E18 sample exhibits increasingly severe plastic deformation as the applied weight increases and the sliding speed decreases. This is because the oxide layer on the surface has less of a lubricating effect when the abraded sample slides under the ball at a slower rate as the sliding speed decreases (Ref 38). A protective oxide layer is typically formed on the surfaces of the sliding materials when the sliding speed is increased when metallic materials are being moved in an oxygen-rich environment, and this oxide film results in a significant reduction in the specific wear rate. Increased applied loads cause single-sided loads to cause more damage and crack thin oxide coatings that have comparatively poor mechanical characteristics in comparison with metals. (Ref 39, 40). As can be observed from the SEM image, there are areas of this sample's surface that have larger deformations. The amount of oxide is observed to decrease as the color changes from dark to white, despite the fact that the oxide density is larger in the black parts of the image. The density of the Cr element is notable in areas with low levels of oxidation. This indicates that the Cr_2O_3 layer created on the surface is more resistant than the ferric oxyhydroxide (FeO(OH)) layer, which is the primary oxide formed in steels, as a result of the 11.5% Cr value observed in AISI D3 steel (Ref 41-43). The variation in wear parameters can be used to explain why the region expressed as Pt 2 is closer to the wear surface in this sample.

EDS analyses performed on SEM images in Fig. 9 (Pt 1), Fig. 10 (Pt 1 and Pt 4), and Fig. 11 (Pt 1) indicate the presence of up to 30% O_2 in certain regions, suggesting an oxidation wear mechanism. The detection of Fe and Cr in EDS analyses, consistent with the composition of AISI D3 steel, implies that the formed oxides are likely iron oxide and chromium oxide.

By lowering the sliding speed to 100 mm/s, the E18 sample exhibits a similar wear process, as shown in Fig. 11. However, it was seen that the oxidation zones were further harmed and the wear worsened in this area. The amount of surface oxidation rose greater under these experimental circumstances. In actuality, it was observed that this sample had the greatest O_2 levels when the EDS analyses were performed. This can be
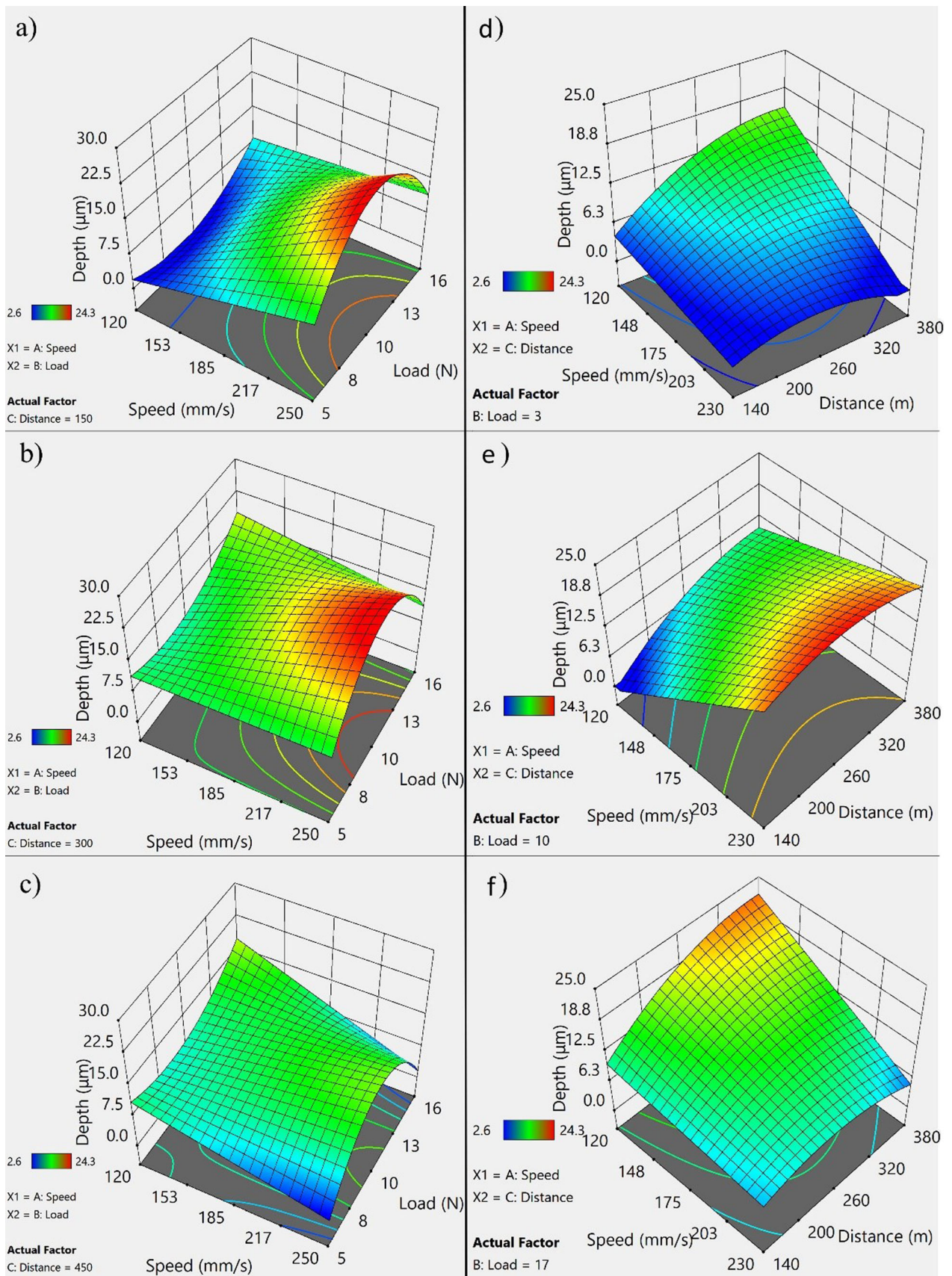
Fig. 5 3-D response surface plot of wear track depth model for constant values of *D* at (a) 150 m, (b) 300 m, (c) 450 m and *L* at (d) 3 N, (e) 10 N, (f) 17 N
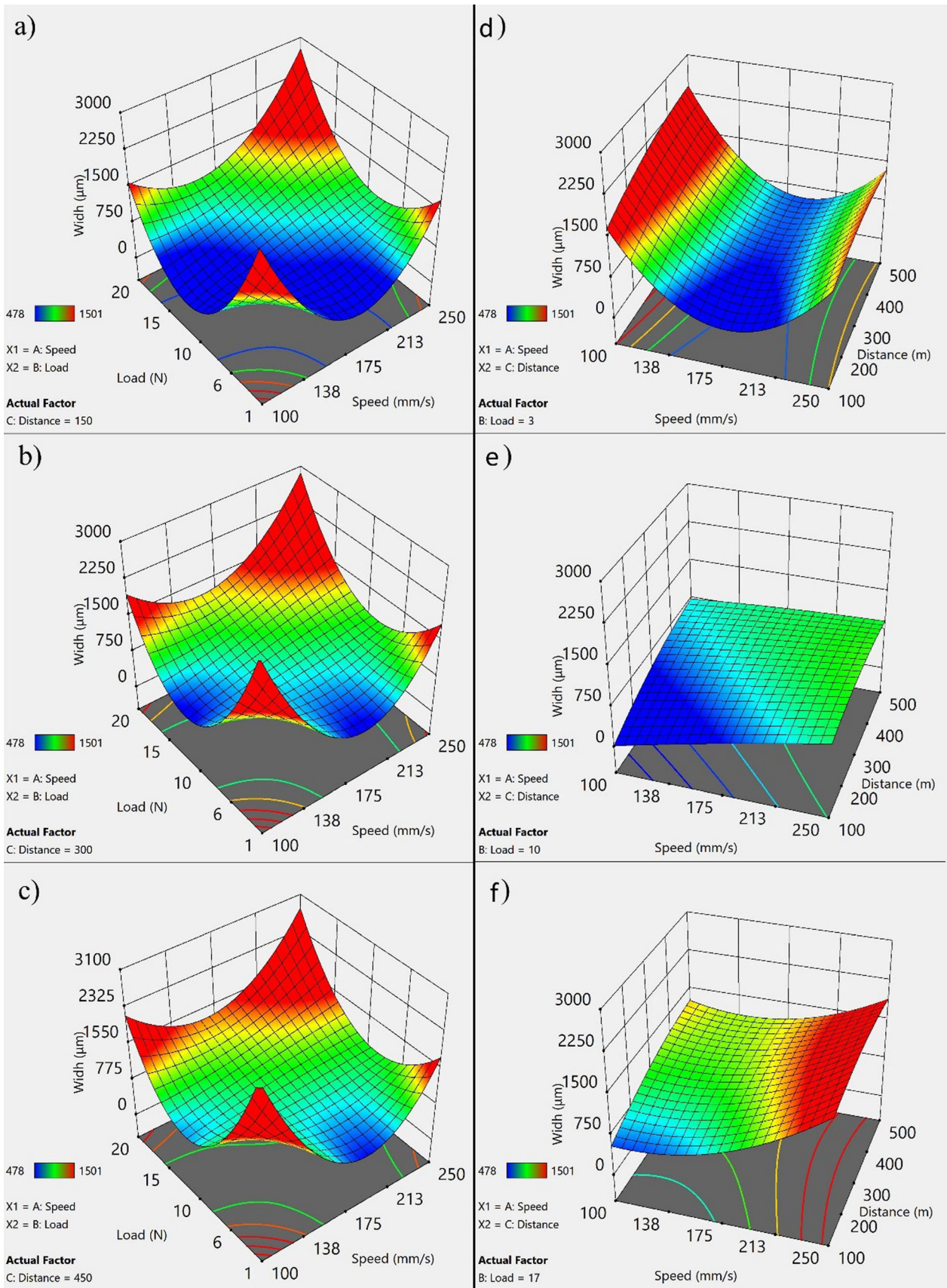
Fig. 6 3-D response surface plot of wear track width model for constant values of *D* at (a) 150 m, (b) 300 m, (c) 450 m and *L* at (d) 3 N, (e) 10 N, (f) 17 N
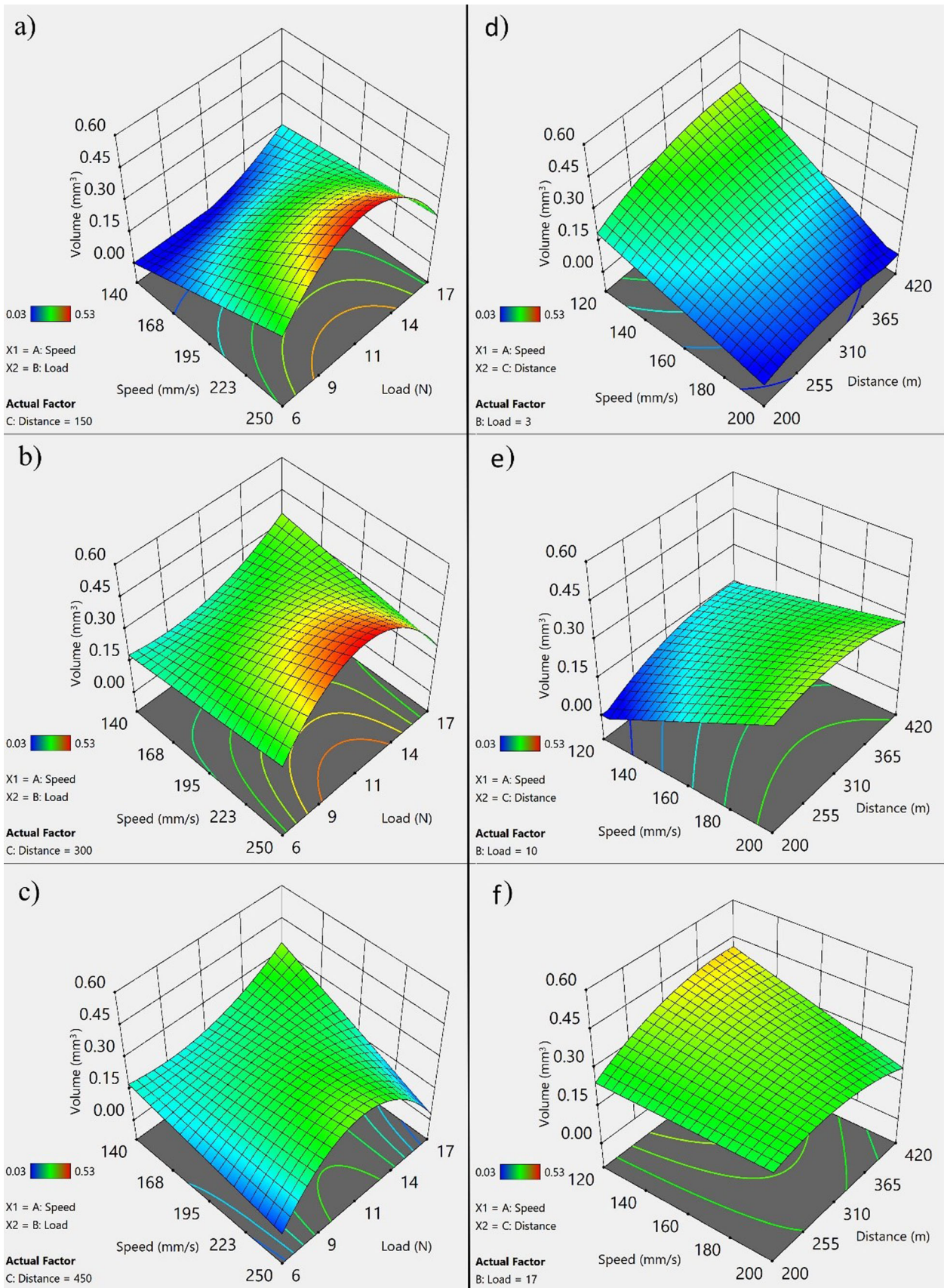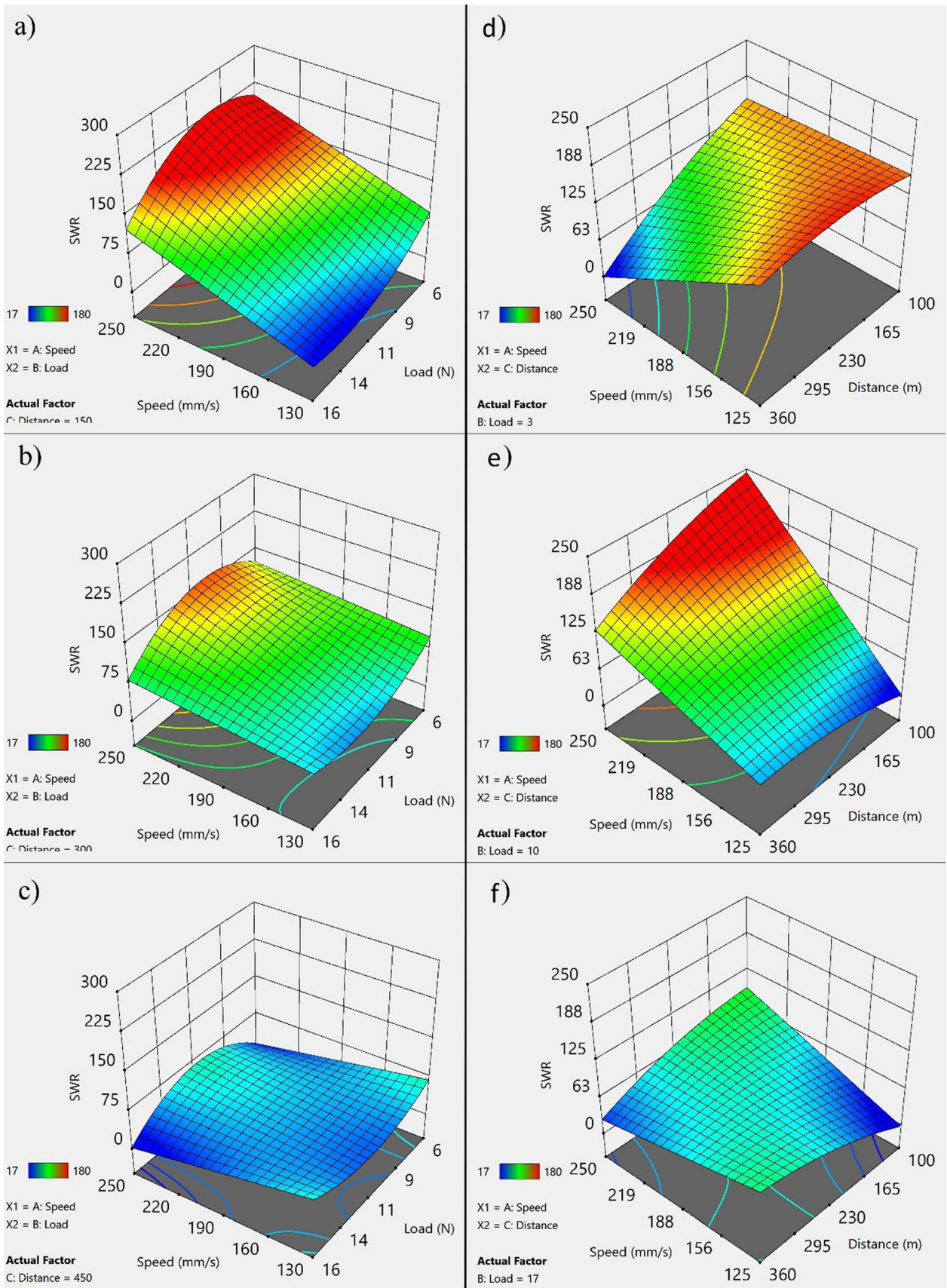
Fig. 7 3-D response surface plot of volume loss model for constant values of *D* at (a) 150 m, (b) 300 m, (c) 450 m and *L* at (d) 3 N, (e) 10 N, (f) 17 N

Fig. 8 3-D response surface plot of wear rate model for constant values of *D* at (a) 150 m, (b) 300 m, (c) 450 m and *L* at (d) 3 N, (e) 10 N, (f) 17 N
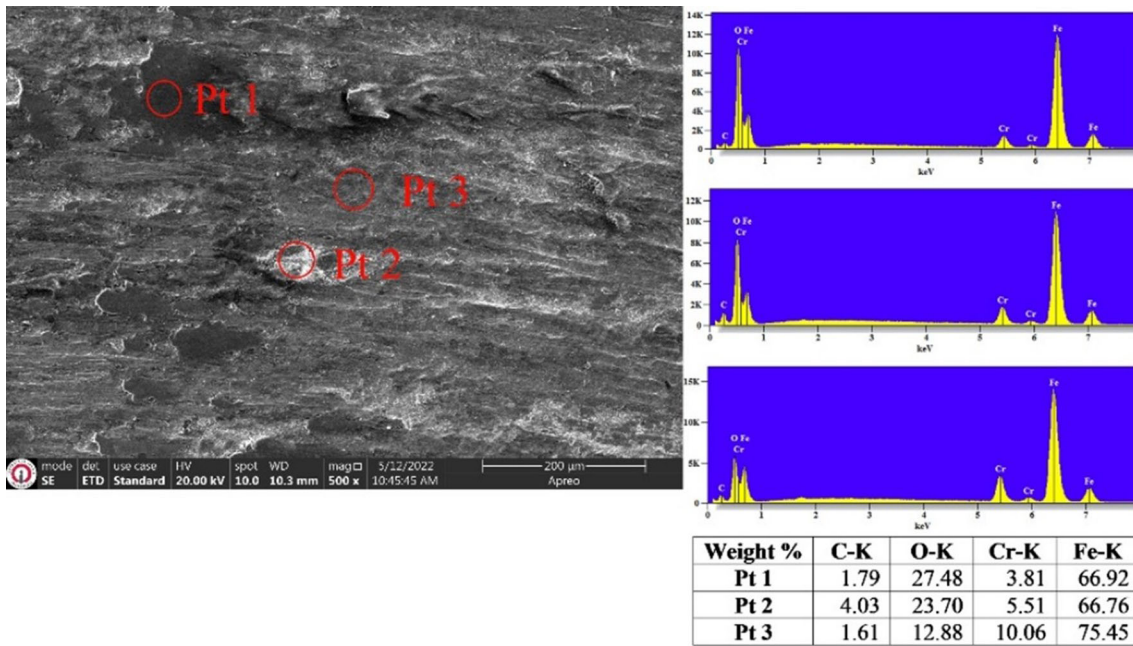
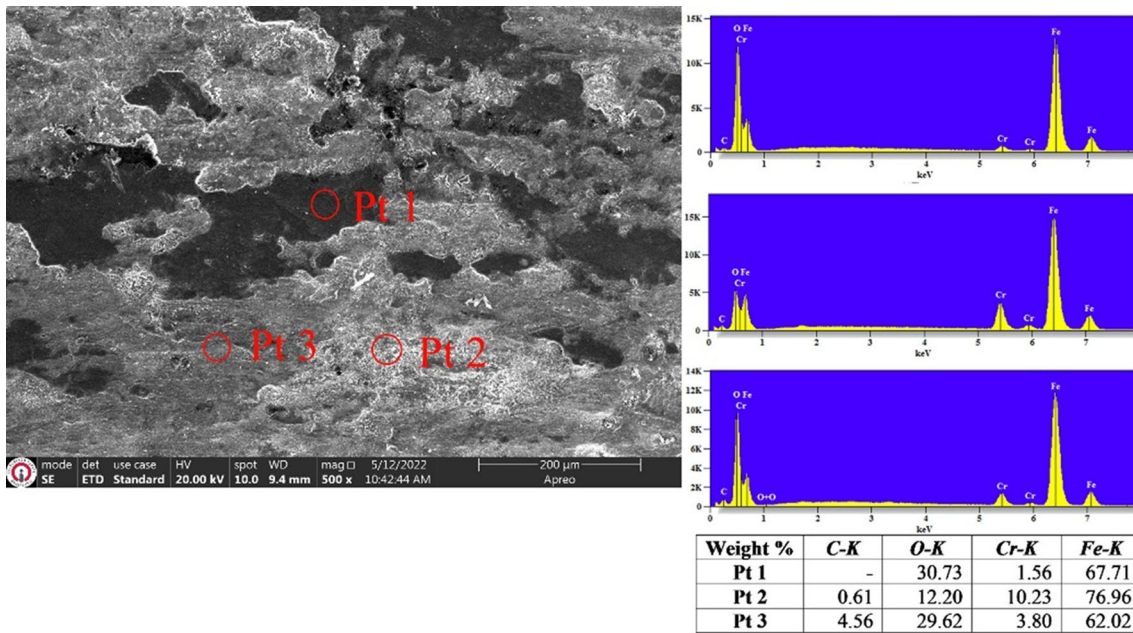**Fig. 9** SEM image and EDS analysis of worn area of sample E 10 (s = 219.6 mm/s, L = 4.85 N, D = 181.08 m)

Weight %	C-K	O-K	Cr-K	Fe-K
Pt 1	1.79	27.48	3.81	66.92
Pt 2	4.03	23.70	5.51	66.76
Pt 3	1.61	12.88	10.06	75.45

Fig. 10 SEM image and EDS analysis of worn area of sample E 18 (s = 175 mm/s, L = 10.5 N, D = 300 m)

Weight %	C-K	O-K	Cr-K	Fe-K
Pt 1	–	30.73	1.56	67.71
Pt 2	0.61	12.20	10.23	76.96
Pt 3	4.56	29.62	3.80	62.02

connected to the wear test parameters because the sample's chemical makeup is the same.

The surface characterization of abrasive balls is another factor used in the understanding of wear mechanisms. Under extreme environmental wear conditions, abrasive balls are more susceptible to damage (Ref 44).

Figure 12 makes it very evident that less damage to the abrasive ball's surface results in reduced material transferring to the ball. The black dot designated as Pt 1's material surface contained abrasion waste that is thought to have been plastered on the ball. Figure 13 shows that although the wear wastes collected more on the ball's surface, the scratches were not

deep, meaning that the ball made of abrasive 52100 steel did not sustain any damage that would have affected the test's outcome. It was found that the weighted balls before and after the wear procedure showed no discernible difference.

5. Conclusions

The study examined the friction and wear behavior properties of AISI D3 material using CCD experimental design and RSM. Factors such as sliding speed, load, and distance were
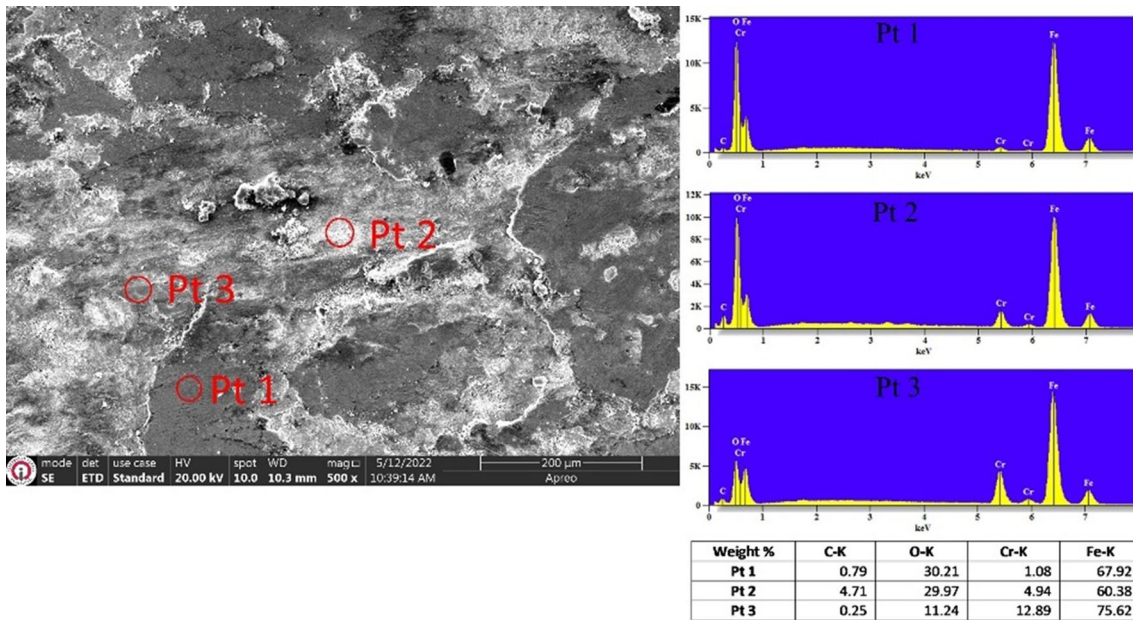
Fig. 11 SEM image and EDS analysis of worn area of sample E 20 (s = 100 mm/s, L = 10.5 N, D = 300 m)
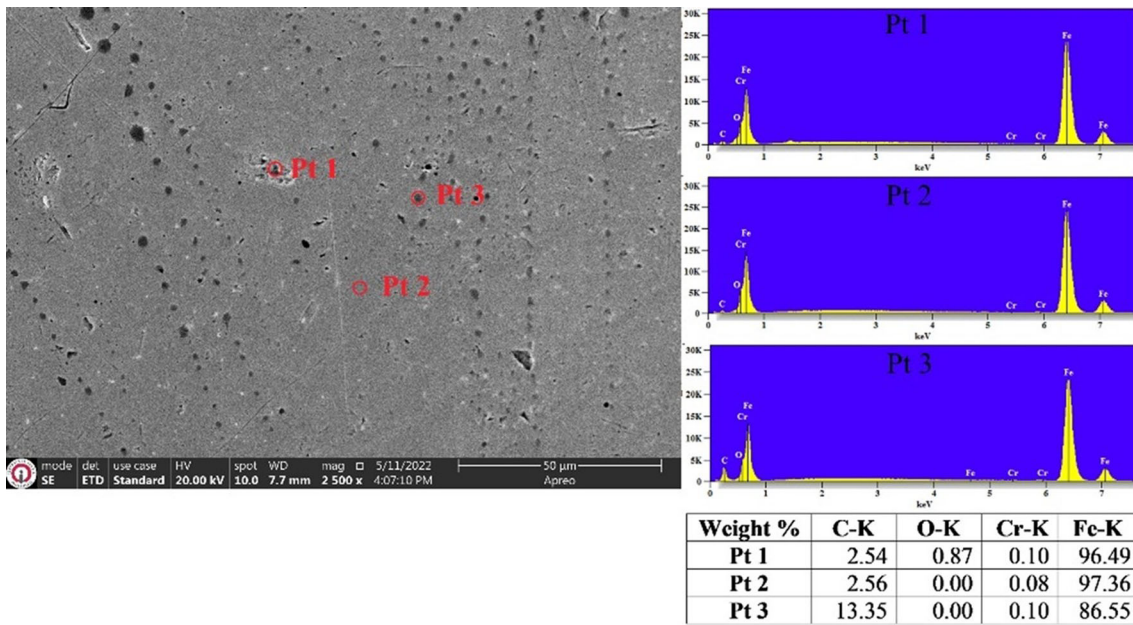
Weight %	C-K	O-K	Cr-K	Fe-K
Pt 1	0.79	30.21	1.08	67.92
Pt 2	4.71	29.97	4.94	60.38
Pt 3	0.25	11.24	12.89	75.62

Fig. 12 SEM images and EDS analysis of unused ball

Weight %	C-K	O-K	Cr-K	Fe-K
Pt 1	2.54	0.87	0.10	96.49
Pt 2	2.56	0.00	0.08	97.36
Pt 3	13.35	0.00	0.10	86.55

analyzed for their effects on COF, wear track depth, track width, volume loss, and wear rate.

The ANOVA analysis revealed that sliding distance had no significant impact on COF, indicating uniformity of the sample for wear testing.

The highest friction coefficient was observed at a load of 1 N and a speed of 100 mm/s. Low friction coefficients were found at loads of 1 and 20 N with high speeds and 12.5 N with low speeds.

Increasing speed resulted in increased track depth at low distance values, while higher distance values led to a decrease in track depth with speed. The low-speed high-distance intersection (120 mm/s, 380 m) showed the deepest wear track under low loads, while the high-speed low-distance intersection (230 mm/s, 140 m) had the least depth.

Load increase shifted the minimum track depth to low speed and low distance, and the maximum to high speed and medium distance, with a similar trend observed in subsequent load increases. Track width generally increased with extreme speed and load values across all distance values. The load had a diminishing effect on other variables until around 10 N, beyond which its impact increased but not as significantly as at low loads (3 N).
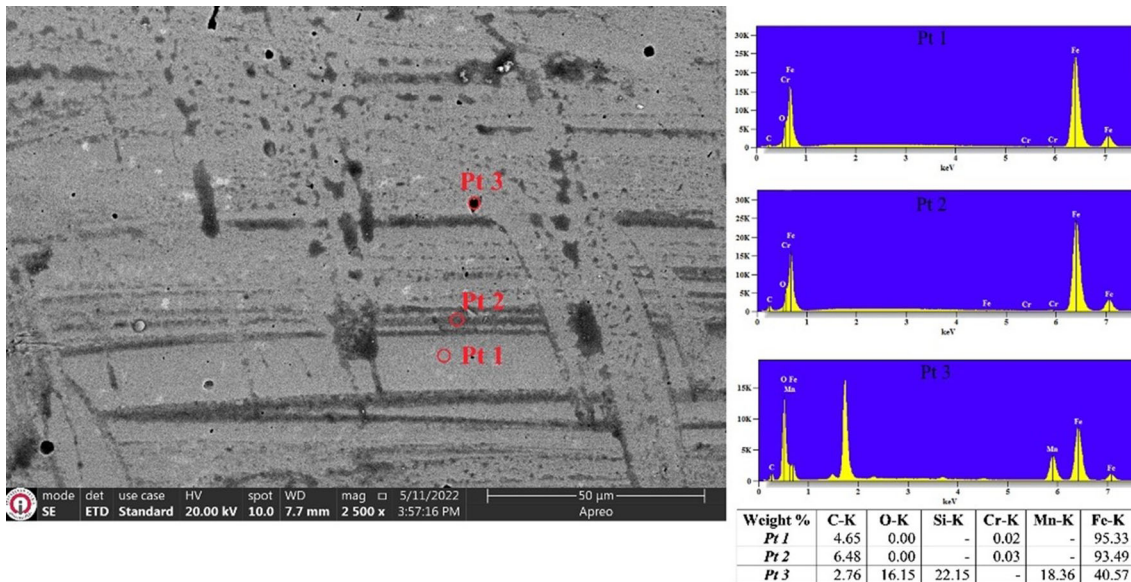
Fig. 13 SEM images and EDS analysis of used ball

Weight %	C-K	O-K	Si-K	Cr-K	Mn-K	Fe-K
Pt 1	4.65	0.00	-	0.02	-	95.33
Pt 2	6.48	0.00	-	0.03	-	93.49
Pt 3	2.76	16.15	22.15	-	18.36	40.57

Volume removal showed a similar pattern to track depth, with load diminishing the effects of the other parameters. As distance increased, load and speed had less impact on wear rate (WR), causing a decrease in WR values overall. At a load of 3 N, the intersection of 360 m distance and 250 mm/s velocity yielded the lowest WR, while at a 10-N load, the 10 m distance shifted to 250 mm/s velocity. Wear rate variance decreased notably with increasing load.

Based on the findings, AISI D3 steel exhibited minimal wear over a sliding distance of 500 m at speeds of 250 mm/s, with loads of 6 and 17 N.

References

1. ASM Handbook Committee, in *ASM Handbook Volume 4A Steel Heat Treating Fundamentals and Processes*, ed. by J.L. Dossett and G.E. Totten, (ASM International, 2013)

2. J.R. Davis, *ASM Specialty Handbook: Stainless Steels*, ASM International, 1994

3. J.R. Davis, *ASM Specialty Handbook: Tool Materials*, ASM international, 1995

4. S. Kumar, M. Nagaraj, N.K. Khedkar, and A. Bongale, Influence of Deep Cryogenic Treatment on Dry Sliding Wear Behaviour of AISI D3 Die Steel, *Mater. Res. Express*, 2018, **5**(11), p 116525. https://doi.org/10.1088/2053-1591/aadeba

5. G.J. Hancock, T. Murray, and D.S. Ellifrit, *Cold-Formed Steel Structures to the AISI Specification*, Taylor & Francis, 2001

6. H.J. Sheikh and T. Singh, Comparative Analysis of Annealed AISI D6 and D2 Cold Working Steel, *Int. J. Res. Appl. Sci. Eng. Technol.*, 2021, **9**(4), p 112–127

7. M.A.S. Bin Abdul Rahim, M. Bin Minhat, N.I.S.B. Hussein, and M.S. Bin Salleh, A Comprehensive Review on Cold Work of AISItool Steel, *Metall. Res. Technol.*, 2018, **115**(1), p 104. https://doi.org/10.1051/metal/2017048

8. A. Kumar, G.D. Thakre, P.K. Arya, and A.K. Jain, Influence of Operating Parameters on the Tribological Performance of Oleic Acid-Functionalized Cu Nanofluids, *Ind. Eng. Chem. Res.*, 2017, **56**(13), p 3527–3541

9. B. Saleh, J. Jiang, A. Ma, D. Song, D. Yang, and Q. Xu, Review on the Influence of Different Reinforcements on the Microstructure and Wear Behavior of Functionally Graded Aluminum Matrix Composites by Centrifugal Casting, *Met. Mater. Int.*, 2020, **26**(7), p 933–960

10. D. Ahmed and M. Mulapeer, Comparison of Specific Wear Rates of Austenitic and Super Austenitic Stainless Steels at High Temperatures, *Zanco J. Pure Appl. Sci.*, 2022, **34**(5), p 20–33

11. D.A. Ahmed and M.M. Mulapeer, Differentiation of Specific Wear Rates of AISI 304 Austenitic and AISI 2205 Duplex Stainless Steels at Room and High Temperatures, *Heliyon*, 2022, **8**(11), p 11807

12. J. Chai and G. Li, Comparative Experiment of Abrasion-Corrosion-Sliding Wear Performance of Two Kinds of Low Alloy Wear-Resistant Steel, *Materials*, 2022, **15**(18), p 6463

13. H.-Y. Lee, Effect of Changing Sliding Speed on Wear Behavior of Mild Carbon Steel, *Met. Mater. Int.*, 2020, **26**(12), p 1749–1756

14. C. Li, X. Deng, and Z. Wang, Friction Behaviour and Self-lubricating Mechanism of Low Alloy Martensitic Steel during Reciprocating Sliding, *Wear*, 2021, **482–483**, p 203972

15. B. Aktas, V. Balak, and C. Carboga, Dry Sliding Wear Behavior of Boron-Doped AISI 1020 Steels, *Acta Phys. Pol. A*, 2017, **132**(3), p 455–457

16. C. Carboga, B. Aktas, and B. Kurt, Dry Sliding Wear Behavior of Boron-Doped 205 Manganese Steels, *J. Mater. Eng. Perform.*, 2020, **29**(5), p 3120–3126

17. B. Aktaş, M. Toprak, A. Çalık, and A. Tekgüler, Effect of Pack-Boriding on the Tribological Behavior of Hardox 450 and HiTuf Steels, *Rev. Adv. Mater. Sci.*, 2020, **59**(1), p 314–321

18. Y. Kayalı, E. Kanca, and A. Günen, Effect of Boronizing on Microstructure, High-Temperature Wear and Corrosion Behavior of Additive Manufactured Inconel 718, *Mater. Charact.*, 2022, **191**, p 112155

19. A. Günen, B. Soylu, and Ö. Karakaş, Titanium Carbide Coating to Improve Surface Characteristic Wear and Corrosion Resistance of Spheroidal Graphite Cast Irons, *Surf. Coat. Technol.*, 2022, **437**, p 128280

20. R. Márquez-Cortés, J. Martínez-Trinidad, M. Flores-Martínez, M. Flores-Jiménez, and R.A. García-León, Sliding Wear Resistance of Borided AISI 4140 Steel, *J. Mater. Eng. Perform.*, 2022, **2022**, p 1–13

21. R.A. García-León, J. Martínez-Trinidad, A. Guevara-Morales, I. Campos-Silva, and U. Figueroa-López, Wear Maps and Statistical Approach of AISI 316L Alloy under Dry Sliding Conditions, *J. Mater. Eng. Perform.*, 2021, **30**(8), p 6175–6190

22. V.V. Reddy, R.K. Mandava, V. Ramakoteswara Rao, and S. Mandava, Optimization of Dry Sliding Wear Parameters of Al 7075 MMC's Using Taguchi Method, *Mater. Today Proc.*, 2022, **62**, p 6684–6688

23. M. Davanageri, S. Narendranath, and R. Kadoli, Dry Sliding Wear Behavior of Super Duplex Stainless Steel AISI 2507: A Statistical Approach, *Arch. Found. Eng.*, 2016, **16**(4), p 47–56

24. R.N. Elshaer, M.K. El-Fawakhry, T. Mattar, and A.I.Z. Farahat, Mathematical Modeling of Wear Behavior and Abbott Firestone Zones

of 0.16C Steel Using Response Surface Methodology, *Sci. Rep.*, 2022, **12**(1), p 14472

25. F. Çavdar, A. Günen, E. Kanca, Y. Er, M.S. Gök, I. Campos-Silva, and M. Olivares-Luna, An Experimental and Statistical Analysis on Dry Sliding Wear Failure Behavior of Incoloy 825 at Elevated Temperatures, *J. Mater. Eng. Perform.*, 2022, **2022**, p 1–24

26. R.A. García-León, J. Martínez-Trinidad, I. Campos-Silva, U. Figueroa-López, and A. Guevara-Morales, Wear Maps of Borided AISI 316L Steel under Ball-on-Flat Dry Sliding Conditions, *Mater. Lett.*, 2021, **282**, p 128842. https://doi.org/10.1016/j.matlet.2020.128842

27. I. Uygur, H. Gerengi, Y. Arslan, and M. Kurtay, The Effects of Cryogenic Treatment on the Corrosion of AISI D3 Steel, *Mater. Res.*, 2015, **18**(3), p 569–574

28. A. Günen, Ö.S. Bölükbaşı, Y. Özgürlük, D. Özkan, O. Odabaş, and İ Somunkıran, Effect of Cr Addition on Properties and Tribological Behavior at Elevated Temperature of Boride Layers Grown on Borosintered Powder Metallurgy Alloys, *Met. Mater. Int.*, **2022**, p 1–19

29. M. Waseem, B. Salah, T. Habib, W. Saleem, M. Abas, R. Khan, U. Ghani, and M.U. Siddiqi, Multi-Response Optimization of Tensile Creep Behavior of PLA 3D Printed Parts Using Categorical Response Surface Methodology, *Polymers*, 2020, **12**, p 2962

30. T. Widyaningsih, S. Waziiroh, E. Wijayanti, and N. Maslukhah, Pilot Plant Scale Extraction of Black Cincau (Mesona Palustris BL) Using Historical-Data Response Surface Methodology, *Int. Food Res. J.*, 2018, **25**, p 12–719

31. I. Dinov, F Distribution Tables 2020, p 1, http://www.socr.ucla.edu/applets.dir/f_table.html. Accessed 4 Feb 2021

32. DYu. Pimenov, A.T. Abbas, M.K. Gupta, I.N. Erdakov, M.S. Soliman, and M.M. el Rayes, Investigations of Surface Quality and Energy Consumption Associated with Costs and Material Removal Rate during Face Milling of AISI 1045 Steel, *Int. J. Adv. Manuf. Technol.*, 2020, **107**(7), p 3511–3525. https://doi.org/10.1007/s00170-020-05236-7

33. S. Mohammed, Z. Zhang, and R. Kovacevic, Optimization of Processing Parameters in Fiber Laser Cladding, *Int. J. Adv. Manuf. Technol.*, 2020, **111**(9), p 2553–2568. https://doi.org/10.1007/s00170-020-06214-9

34. L. da Conceição and A.S.C.M. D'Oliveira, The Effect of Oxidation on the Tribolayer and Sliding Wear of a Co-Based Coating, *Surf. Coat. Technol.*, 2016, **288**, p 69–78

35. M.X. Wei, K.M. Chen, S.Q. Wang, and X.H. Cui, Analysis for Wear Behaviors of Oxidative Wear, *Tribol. Lett.*, 2011, **42**(1), p 1–7

36. A. Gunen, M. Ulutan, M.S. Gok, B. Kurt, and N. Orhan, Friction and Wear Behaviour of Borided Aisi 304 Stainless Steel With Nano Particle and Micro Particle Size of Boriding Agents, *J. Balkan Tribol. Assoc.*, 2014, **2014**, p 362–379

37. Q.Y. Zhang, K.M. Chen, L. Wang, X.H. Cui, and S.Q. Wang, Characteristics of Oxidative Wear and Oxidative Mildwear, *Tribol. Int.*, 2013, **61**, p 214–223

38. L.J. O'Donnell, G.M. Michal, F. Ernst, H. Kahn, and A.H. Heuer, Wear Maps for Low Temperature Carburised 316L Austenitic Stainless Steel Sliding against Alumina, *Surf. Eng.*, 2010, **26**(4), p 284–292

39. I. Campos-Silva, M. Palomar-Pardavé, R. Pérez Pastén-Borja, O. KahveciogluFeridun, D. Bravo-Bárcenas, C. López-García, and R. Reyes-Helguera, Tribocorrosion and Cytotoxicity of FeB-Fe2B Layers on AISI 316 L Steel, *Surf. Coat. Technol.*, 2018, **349**, p 986–997

40. A. Erdogan, B. Kursuncu, A. Günen, M. Kalkandelen, and M.S. Gok, A New Approach to Sintering and Boriding of Steels "Boro-Sintering": Formation Microstructure and Wear Behaviors, *Surf. Coat. Technol.*, 2020, **386**, p 125482

41. K. Xiao, C. Dong, X. Li, and F. Wang, Corrosion Products and Formation Mechanism during Initial Stage of Atmospheric Corrosion of Carbon Steel, *J. Iron. Steel Res. Int.*, 2008, **15**(5), p 42–48

42. L. Cáceres, T. Vargas, and L. Herrera, Influence of Pitting and Iron Oxide Formation during Corrosion of Carbon Steel in Unbuffered NaCl Solutions, *Corros. Sci.*, 2009, **51**(5), p 971–978

43. J.G. Castaño, C.A. Botero, A.H. Restrepo, E.A. Agudelo, E. Correa, and F. Echeverría, Atmospheric Corrosion of Carbon Steel in Colombia, *Corros. Sci.*, 2010, **52**(1), p 216–223

44. G.B. Stachowiak, G.W. Stachowiak, and J.M. Brandt, Ball-Cratering Abrasion Tests with Large Abrasive Particles, *Tribol. Int.*, 2006, **39**(1), p 1–11